PCCP

RSC Publishing

PAPER

# Atomic pair distribution functions analysis of disordered low-*Z* materials

Cite this: *Phys. Chem. Chem. Phys.*, 2013, **15**, 8544

V. Petkov,*[a] Y. Ren,[b] S. Kabekkodu[c] and D. Murphy[d]

Received 25th September 2012,
Accepted 11th December 2012

DOI: 10.1039/c2cp43378h

**www.rsc.org/pccp**

Results of high-energy X-ray diffraction experiments coupled to atomic pair distribution function analysis of disordered low-*Z* materials are presented. Several scientifically and technologically important classes of disordered low-*Z* materials such as small and large organic molecules, graphitic powders, polymers and liquids are intentionally explored to certify the technique's performance. Results clearly show that disordered low-*Z* materials can be well characterized in terms of material's phase identity, relative abundance in mixtures and atomic-scale structure. The demonstrated efficiency of the technique provides the scientific community with much needed confidence to apply it more often than now.

## 1. Introduction

Phase identity, relative abundance in mixtures and atomic-scale structure are important material characteristics both from a scientific and technological point of view. Traditionally they are obtained by Bragg X-ray diffraction (XRD). Traditional XRD, however, is straightforwardly applicable only to crystalline materials. Many materials of scientific and technological importance are structurally disordered and not amenable to Bragg X-ray diffraction. Further complications arise when disordered materials are made of low-*Z* ($Z < 10$) atomic species since those scatter X-rays rather weakly. High-energy XRD coupled to atomic Pair Distribution Function (PDF) analysis has proven very successful in characterizing disordered high-*Z* materials from glasses and nanoparticles to crystals with intrinsic disorder.[1–4] Examples of the application of the technique on disordered low-*Z* materials are, however, scattered posing questions about its efficiency with such materials. In this paper we show several examples of high-energy XRD and atomic PDFs studies on disordered low-*Z* materials. The examples deliberately cover various classes of disordered low-*Z* materials including nanocrystalline derivatives of cellulose, very fine graphitic powders, small organic molecules used as pharmaceuticals or for energy harvesting, polymers and liquids. We demonstrate that high-energy XRD coupled to atomic PDFs analysis can be as efficient with disordered low-*Z* materials as it is with high-*Z* ones providing the scientific community with much needed confidence to apply this non-traditional technique more often than now.

[a] *Department of Physics, Central Michigan University, Mt. Pleasant, MI 48859, USA. E-mail: petko1vg@cmich.edu*
[b] *X-ray Science Division, Advanced Photon Source, Argonne National Laboratory, Argonne, IL 60439, USA*
[c] *International Centre for Diffraction Data, 12 Campus Blvd., Newtown Square, PA 19073-3273, USA*
[d] *Bristol-Myers Squibb Co., Drug Product Science and Technology, New Brunswick, NJ 08903, USA*

## 2. Experimental

### 2.1 Samples

All samples studied here are of high purity standards obtained from reliable commercial sources such as Aldrich (graphitic powders, cellulose and trehalose, $C_{60}$, ammonia borane), Bristol-Myers Squibb (indomethacin and polyvinylpyrrolidone) and Dendritic Nanotechnologies (7th generation PAMAM dendrimers).

### 2.2 High energy X-ray diffraction experiments

Most high-energy XRD experiments were carried out at the 11-ID-C beamline at the Advanced Photon Source using X-rays with an energy of 115.232 keV ($\lambda$ = 0.1076 Å) and a large-area (mar345) detector. Synchrotron radiation X-rays were used for two reasons. Firstly, the higher flux of synchrotron radiation X-rays makes it possible to measure the rather diffuse diffraction patterns of disordered low-*Z* materials with a very good statistical accuracy. Secondly, the higher energy of the synchrotron radiation X-rays used makes it possible to reach higher wave-vectors, *Q*, which is essential for the atomic PDF analysis. With the present experiments diffraction data were collected to wave vectors as high as 25 Å$^{-1}$. For the experiments, samples were loaded in thin walled glass capillaries. Empty capillaries were also measured to estimate the overall background scattering (capillary plus air). A few selected samples, in particular indomethacin and polyvinylpyrrolidone, were also measured with higher-energy X-rays produced by in-house equipment using

Ag Kα radiation ($E$ = 22 keV; $\lambda$ = 0.56 Å) and a single point (scintillator) detector. These samples were also loaded in thin walled glass capillaries and data taken to wave vector as high as 20 Å$^{-1}$.

### 2.3 Basics of the atomic PDFs analysis

The frequently used reduced atomic PDF, $G(r)$, gives the number of atoms in a spherical shell of unit thickness at a distance $r$ from a reference atom as follows:

$$G(r) = 4\pi r[\rho(r) - \rho_o] \quad (1)$$

where $\rho(r)$ and $\rho_o$ are the local and average atomic number densities, respectively. It is a one-dimensional function that oscillates around zero showing positive peaks at distances separating pairs of atoms, *i.e.* where the local atomic density exceeds the average one. As demonstrated in the examples below the oscillations are characteristic of the particular phase state and atomic-scale structure of disordered low-$Z$ material studied. The atomic PDF $G(r)$ is an experimentally assessable quantity since any condensed material can act as a diffraction grating when irradiated with X-rays producing a diffraction pattern that is a Fourier transform of the distribution of the *distinct* atomic pair distances in that material/grating.[4] Therefore, by collecting an X-ray diffraction (XRD) pattern and Fourier transforming it, the distribution of the atomic pair distances can be obtained for any condensed material, be it crystalline or not. In particular, the atomic PDF $G(r)$ is the exact Fourier transform of the structure sensitive part of the scattered X-ray intensities, also known as structure function, $S(Q)$, *i.e.*

$$G(r) = (2/\pi) \int_{Q=Q_{min}}^{Q_{max}} Q[S(Q) - 1] \sin(Qr) \mathrm{d}Q, \quad (2)$$

where $Q$ is the magnitude of the wave vector ($Q = 4\pi \sin\theta/\lambda$), $2\theta$ is the angle between the incoming and outgoing X-rays and $\lambda$ is the wavelength of the X-rays used.[5] Note that the structure function, $S(Q)$, is related to only the coherent/elastic part of the scattered X-ray intensities, $I^{coh.}(Q)$, as follows:

$$S(Q) = 1 + [I^{coh.}(Q) - \Sigma c_i |f_i(Q)|^2]/|\Sigma c_i f_i(Q)|^2, \quad (3)$$

where $c_i$ and $f_i(Q)$ are the atomic concentration and the X-ray scattering factor, respectively, for the atomic species of type $i$. Other definitions of $S(Q)$ and the atomic PDF are also known but less frequently used.[6] Therefore, to obtain an experimental atomic PDF (i) an XRD data set should be collected to high-wave vectors, (ii) only the coherent part, $I^{coh.}(Q)$, of it extracted, (iii) reduced to a structure factor $S(Q)$ (eqn (3)) and (iv) then Fourier transformed (eqn (2)) to a PDF. For a material comprising $n$ atomic species a single diffraction experiment would yield a total atomic distribution function, $G(r)$, which is a weighted sum of $n(n + 1)/2$ partial PDFs, $G(r_{ij})$, *i.e.*

$$G(r) = \sum_{i,j} w_{ij} G_{ij}(r), \quad (4)$$

where $w_{ij}$ are weighting factors[4–6] depending on the concentration and scattering power of the atomic species as follows:

$$w_{ij} = c_i c_j f_i(Q) f_j(Q)/|\Sigma c_i f_i(Q)|^2. \quad (5)$$

For practical purposes $w_{ij}$'s are often evaluated for $Q = 0$.

Note that the coherent (elastic) scattering of atomic species of the low-$Z$ number is quite weak while the incoherent (Compton) scattering – quite strong[4] rendering the derivation of experimental PDFs from experimental XRD patterns not as easy as it is with high-$Z$ materials. Nevertheless by carefully conducting the XRD data collection and reduction procedures good quality atomic PDFs for disordered low-$Z$ materials can be obtained and used to obtain important material characteristics as demonstrated by the examples below.

## 3. Results and discussion

### 3.1 Cellulose and derivatives

Cellulose is an organic polymer with the formula $(C_6H_{10}O_5)_n$. From a structural point of view it is built of chains of several hundred to over ten thousand D-glucose ($C_6H_{12}O_6$) molecules (see the inset in Fig. 2). It is the most common organic compound on Earth that has many applications in paper, textiles and pharmaceutical industries requiring careful structural characterization of cellulose on a daily basis. Several different crystalline modifications of cellulose and its derivatives are known, differing in the connectivity of the building glucose units. In particular, natural cellulose crystallizes in the so-called type I structure, where two modifications – $I_\alpha$ and $I_\beta$ are known. Regenerated cellulose usually crystallizes in the type II structure.[7] Cellulose acetate ($C_6H_{10}O_5$), that is used as a film base in photography, as a component in some adhesives and as a synthetic fiber, is also made up of chains of glucose molecule units but the side units attached to the glucose molecules are different from those in cellulose (see Fig. 2). Trehalose ($C_{12}H_{22}O_{11}$) can be found in animals, plants, and microorganisms. It is composed of glucose molecules that are linked by oxygen bridges, with the packing of the glucose molecules here is different from that in cellulose (see Fig. 2). Cellulose, cellulose acetate and trehalose, however, are rarely used as crystals. More often than not real life applications are based on their non-crystalline forms that produce the type of XRD patterns shown in Fig. 1. The patterns have strong broad peaks at low diffraction angles followed by a few low amplitude oscillations. Such diffraction patterns are not easy to interpret in the traditional way. When they are reduced to the corresponding atomic PDFs the structural differences between the three glucose-molecules based materials are seen in a much clearer way.

As can be seen in Fig. 2 the experimental PDFs have very sharp peaks at low-$r$ values reflecting interatomic distances within the glucose building molecules and the side chain radicals attached to them. In particular all three PDFs show a strong peak at approximately 1.44 Å due to C–C bonds within the glucose molecules. The cellulose acetate shows a low-$r$ shoulder in the first PDF peak due to the numerous C–H bonds ($\sim$1.1 Å) from the $CH_3$ side units. This shoulder is not seen in the PDFs of nanocrystalline cellulose and amorphous trehalose that show a distinct first peak at 0.98 Å arising from the abundant O–H bond distances in the respective side units. This allows us to immediately differentiate the disordered

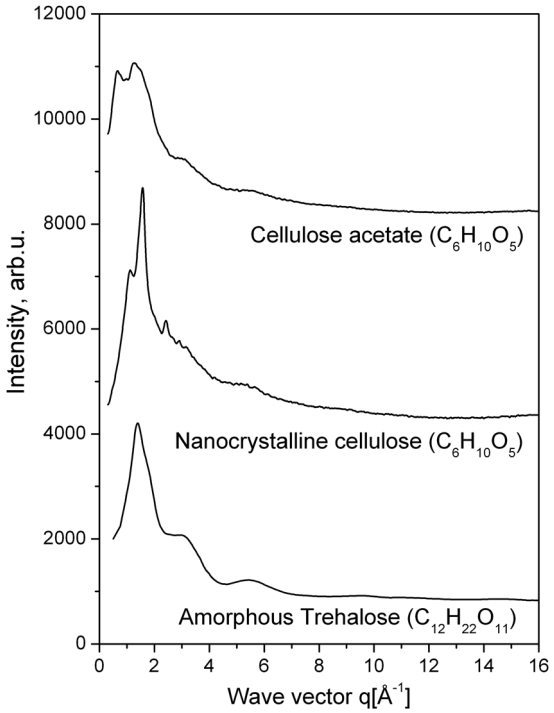


**Fig. 1** Experimental XRD patterns of cellulose acetate thin film, very fine powder cellulose and amorphous trehalose.

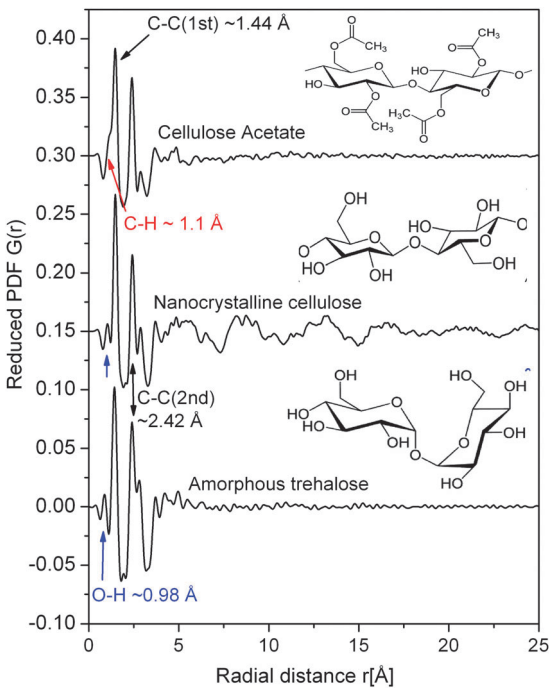


**Fig. 2** Experimental atomic PDFs extracted from the diffraction data of Fig. 1. The molecular glucose unit of cellulose acetate, cellulose and trehalose is shown by the respective data sets. Shortest interatomic distances occurring in these materials are marked by arrows.

modification of cellulose acetate from those of pure cellulose and trehalose. Furthermore, the profiles of the PDFs for cellulose and trehalose distinctly differ from each other for distances longer than 2.5 Å reflecting the different way glucose molecules pack together in these materials. This difference allows an unambiguous differentiation between structurally disordered cellulose and trehalose. Obviously, disordered materials based on glucose molecules can be unambiguously identified thanks to the presence of very distinct features in their atomic PDFs.

Analysis of experimental atomic PDFs also allows determining the particular structure type of disordered materials based on glucose molecules. This can be done, for example, by comparing the experimental PDFs with model ones computed from the structures of the respective crystals. As illustrated in Fig. 3 the experimental PDF for the nanocrystalline cellulose studied here is best described in terms of a structure model based on the Ib crystalline modification[7,8] of cellulose. That of amorphous trehalose is best approximated with a structure model based on the *h*-crystalline modification of trehalose.[9] Note that upon such a comparison an agreement factor $R_w$ defined as:

$$R_w = \left\{ \frac{\sum w_i (G_i^{\text{exp.}} - G_i^{\text{calc.}})^2}{\sum w_i (G_i^{\text{exp.}})^2} \right\}^{1/2}, \qquad (6)$$

where $G^{\text{exp.}}$ and $G^{\text{calc.}}$ are the experimental and calculated PDFs, respectively, and $w_i$ are weighting factors reflecting the quality of the individual data points computed. Such $R_w$'s may appear (see Fig. 3) somewhat high when compared to agreement factors resulted from traditional (*e.g.* Rietveld) analysis of XRD data. This mostly reflects the fact that atomic PDFs take both the sharp, Bragg like features and the diffuse component of the XRD data into account while traditional XRD data analysis considers

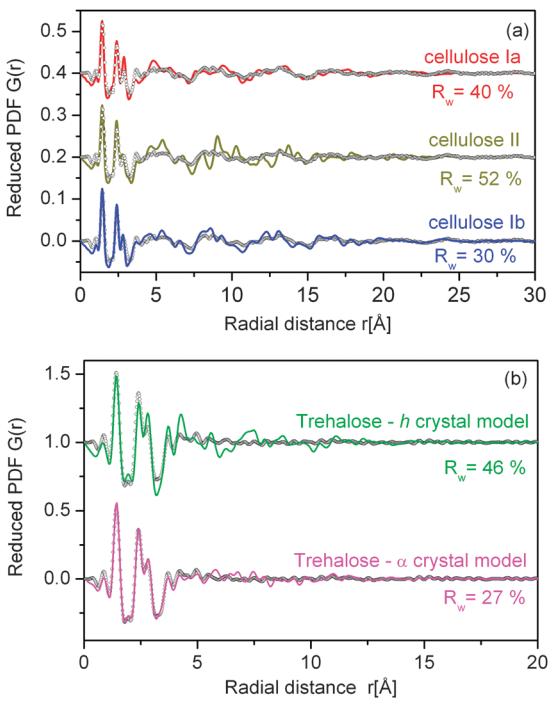


**Fig. 3** Fits to the experimental atomic PDFs of nanocrystalline cellulose and amorphous trehalose (symbols). The fits (solid line) are based on the Ia, Ib and II crystalline phases[7,8] of cellulose, and α and h crystalline phases[9] of trehalose. The respective agreement factors $R_w$ are given by each of the fits.

only the former. The inherently higher absolute value of the agreement factors $R_w$ used in PDFs analysis, however, does not affect their functional purpose as a residuals quantity that allows differentiating between competing structure models.

### 3.2 Disordered graphitic materials

At present a significant research effort is underway worldwide to find advanced negative electrode materials for Li-ion batteries. Graphitic carbon is a material of great interest because it can accommodate Li atoms fast, reversibly and without generating much mechanical stress. Under normal conditions pristine graphitic carbon can accommodate up to one Li atom per six carbon atoms.[10] Real-life applications, however, demand higher Li storage capacities and scientists have been looking into ways to go beyond what bulk $LiC_6$ can offer. Technology friendly routes such as ball milling have shown good promise leading to 2–3 times increase in the Li storage capacity. The increase has been explained in terms of the 'stacks of fallen cards' model which features breaking, upon the impact of ball milling, of the extended graphitic layers into smaller pieces that are randomly oriented with respect to each other, thus posing a diminished steric hindrance for Li to intercalate. The increased Li storage capacity, however, has been found to fluctuate with the milling time, puzzling scientists for more than a decade. High-energy XRD and atomic PDFs analysis allow resolving this puzzle with success. Fig. 4a shows the high-energy XRD pattern of pristine graphitic carbon that has several sharp Bragg peaks as it should be for a micron-sized crystalline material. The peaks are getting progressively broader with milling times to a state where they merge into a few broad humps in the diffraction pattern for 1270 min milled carbon. Bragg peak broadening may come from smaller crystallite sizes, increased lattice strain and/or the presence of a substantial number of structural defects. Traditional XRD, however, is not able to reveal the exact nature of these structural modifications. Here is where the atomic PDFs analysis comes to help. Experimental atomic PDFs are shown in Fig. 4b. Peaks in the respective atomic PDFs occur at distances separating well defined pairs of carbon atoms.

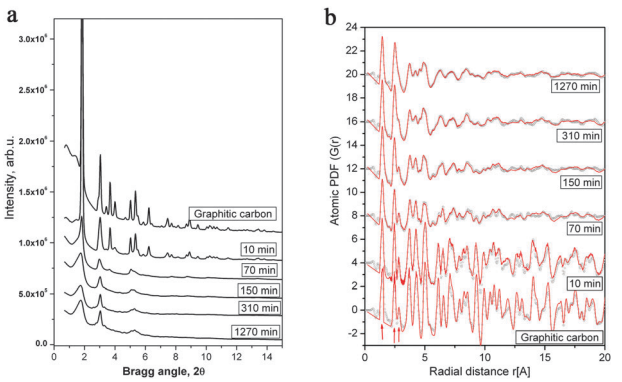


**Fig. 4** (a) Experimental XRD patterns of pristine and ball milled graphitic powders. The respective milling times are given by each dataset. (b). Atomic PDFs extracted from the powder patterns in (a) (symbols) and reverse Monte Carlo fits to them (solid line). Arrows mark the shortest interatomic distances in graphite.

In particular, the first PDF peak in all carbon samples shown in Fig. 4b is positioned at a distance of 1.41 Å, which is the first neighbor ($sp^2$) carbon–($sp^2$) carbon distance in graphite. The PDF for the pristine (*i.e.* not milled) graphitic carbon shows many well-defined peaks extending to long interatomic distances as it should be with polycrystalline materials. The experimental PDF for the sample milled for 10 min is very similar to that of the not-milled one indicating that short milling times hardly affect the atomic-scale structure of graphitic carbon, except for breaking the graphitic layers into smaller pieces. Milling for longer times, however, affects it considerably since the PDF peaks, *i.e.* the atomic coordination spheres they reflect, start losing their sharpness leading to a reduction of the length of structural coherence, measured by the real space distance at which the PDF data decay to zero, to only 20–30 Å. Indeed the atomic PDFs for graphitic carbon milled for 70–1270 min resemble very much those of low crystallinity carbon obtained by a thermal decomposition of organic precursors.[11] The graphitic planes in those low crystallinity carbons have been found to be rich in structural defects and heavily buckled. For the samples studied here this atomic-scale picture is confirmed in very good detail by reverse Monte Carlo simulations[11] (see Fig. 4b). They show that the graphitic layers are perfect and well lined up in the not-milled samples only. Carbon atoms in the 10 min milled sample (Fig. 5(b)) are somewhat displaced out of the initially perfectly flat graphitic layers. Some missing atom-type vacancies appear on the layers as well. With the samples milled for longer times more and more carbon atoms move further and further out of the graphitic layers opening extended missing atom-type vacancies on them (see Fig. 5(e) and (f)).

Some of the atoms displaced from the layers end up trapped in between the layers, turning the carbon milled for 310 and 1270 min into an assembly of heavily distorted (out-of-plane), defective (missing atoms) and locally fused together graphitic layers (see Fig. 5). Results from this study show that the 'stack of fallen cards' model is valid for graphitic carbon milled for only very short times. The graphitic planes in such carbon do break into smaller pieces and remain rather flat. As a result Li atoms can easily be accommodated in between the layers, at the edges of smaller size layers and at defect sites within the layers resulting in an increased Li storage capacity.[11] The graphitic layers in carbon milled for longer times, however, become too buckled and locally fused together (see Fig. 5(e) and (f)) making it increasingly difficult for Li to intercalate in between them. As a result the lithium storage capacity drops substantially.[10] To increase it other technological routes that not only yield very fine size graphitic platelets but also retain their out-of-plane structural integrity have to be explored. Atomic PDFs analysis will be indispensable in this line of research.

Modern technology uses carbon not only in its graphitic form. Several others, mostly nanophase forms of carbon such as graphene sheets, mesoporous carbon, carbon nanotubes and $C_{60}$ fullerene find many applications in bio-sciences[12] and energy harvesting.[13]

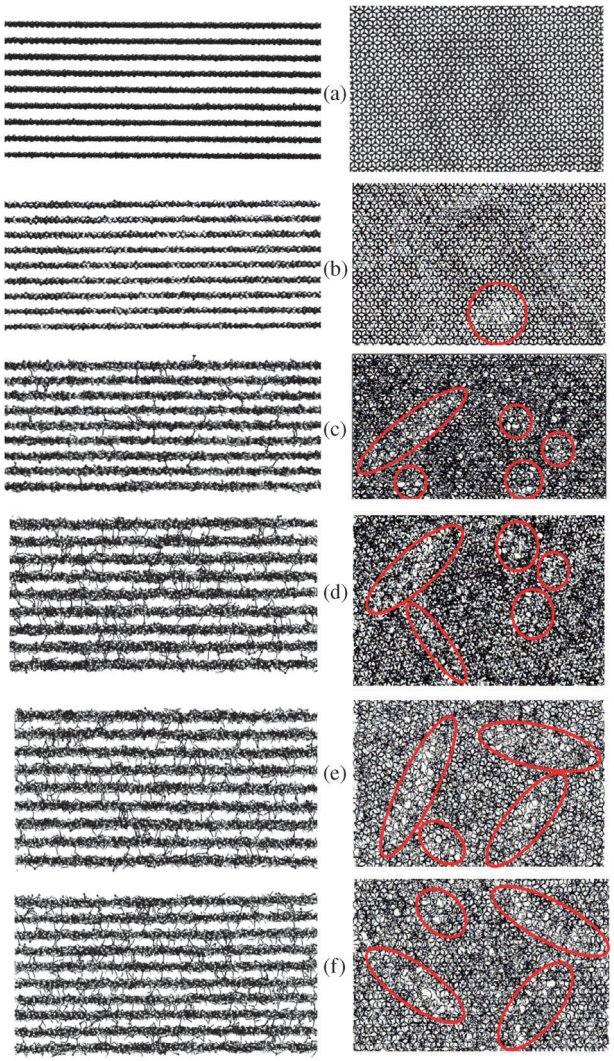


**Fig. 5** Fragments of the RMC constructed models of graphitic carbon guided by the experimental PDF data (see Fig. 4b). Lateral view is shown on the left and top view of the layers – on the right. Pristine state is shown in (a) and ball-milled for 10 min in (b), for 70 min in (c), for 150 min in (d), for 310 min in (e) and for 1270 min in (f). Circles and ellipses (right panel, in red) mark the extended planar defects (missing atoms) in the graphitic planes of the ball-milled samples.

Experimental high-energy XRD patterns of graphitic carbon and several carbon nanophases are shown in Fig. 6. The diffraction data show a few sharp features at low Bragg angles followed by hardly discernible, low frequency oscillations. The respective atomic PDFs, however, are rich in distinct features allowing an unambiguous identification of the different carbon nanophases.

For example, the first two peaks in the experimental PDFs in Fig. 7 are centered at 1.41 Å and 2.42 Å corresponding to the two shortest distances between carbon atoms sitting on the vertices of hexagonal rings, confirming the $(sp^2)$–$(sp^2)$ bonding in all carbon nanophases studied here. Beyond the first and second peaks/coordination sphere, however, the experimental PDF shows distinctly different behavior coming from the different ways carbon atoms arrange at longer interatomic distances. The PDFs for single carbon nanotubes and mesoporous carbon

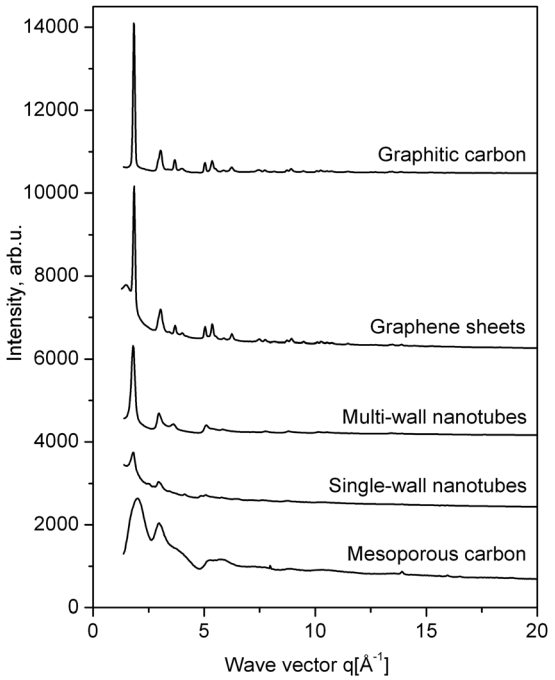


**Fig. 6** Experimental XRD patterns of crystalline graphitic carbon (top) and several carbon nanophases.

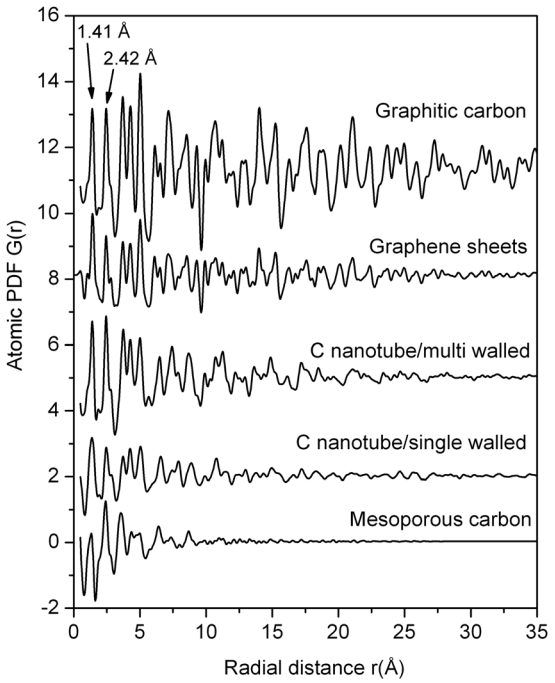


**Fig. 7** Experimental atomic PDFs of crystalline graphitic carbon (top) and several carbon nanophases.

decay to zero very fast reflecting the presence of single sheets of hexagonally coordinated carbons in both materials. The sheets are folded in a circular manner with the nanotubes and remain flat and riddled with extended defects (missing atoms) with the mesoporous carbon, respectively. This difference renders the respective PDFs different. On the other hand, the PDFs for

multiwalled carbon nanotubes and stacks of graphene nanosheets decay to zero at much longer interatomic distances due to the multiscroll nature of the former and the lack of structural defects in the latter. The PDF peaks at these longer distances are, however, different again due to the different local symmetry of the respective nanophases: inherently circular with the tubes and extended planar with nanosheets. Obviously by comparing experimental PDFs various carbon nanophases of current scientific and technological interest can be identified unambiguously. The identification can be greatly facilitated if the experimental PDFs are stored in a database and subjected to search/match algorithms of the type employed in the powder diffraction file with XRD patterns for polycrystalline materials.[14,15]

### 3.3 Small organic molecules used in the pharmaceutical industry

At present the pharmaceutical industry is facing a revolution involving a transformation from crystalline to non-crystalline drug formulations taking advantage of the improved solubility of the latter. Intensive research has been going on to characterize such non-crystalline drug formulations and mixtures.[16,17] A typical example considered below is a mixture of the drug indomethacin ($C_{19}H_{16}ClNO_4$) with polyvinylpolypyrrolidone $(C_6H_9NO)_n$ obtained by fast co-spraying. This technological route allows for a better mixing of the two materials resulting in an improved thermal stability and solubility.

Experimental XRD patterns for crystalline indomethacin, spray dried indomethacin and polyvinylpyrrolidone (PVP) as well as mixtures of co-dried indomethacin and PVP are shown in Fig. 8. Crystalline indomethacin exhibits a series of sharp Bragg peaks that almost disappear when the material is fast dried. The XRD pattern of dried PVP is also almost featureless indicating a heavily disordered structural state. The XRD patterns of the mixtures of spray co-dried indomethacin and PVP do not show any well-defined diffraction features indicating a completely amorphous structural state. When the XRD patterns are converted into the corresponding atomic PDFs distinct peaks appear allowing unambiguous quantitative and qualitative identification of the different non-crystalline phases. The atomic PDFs for crystalline indomethacin and sprayed PVP show a characteristic sequence of low-*r* peaks coming from the intact molecular units building these materials (Fig. 9a). The peaks have different intensity. Besides, the PDF for crystalline indomethacin shows a series of higher order peaks, allowing a clear differentiation between it and sprayed PVP.

The differentiation can be clearly done using synchrotron or in-house data with the resolution of the latter is slightly compromised due the shorter wavelength (0.56 Å *vs.* 0.1015 Å) used. Obviously going to synchrotron radiation sources is not always necessary when qualitative characterization of disordered low-*Z* materials is needed.

A closer look at the experimental atomic PDFs (see Fig. 9b) reveals a systematic evolution of the intensity of the first three PDFs peaks with the relative indomethacin/PVP ratio. These peaks are marked with horizontal arrows in Fig. 9b and given on an enlarged scale in Fig. 10a. The relative ratio of either the

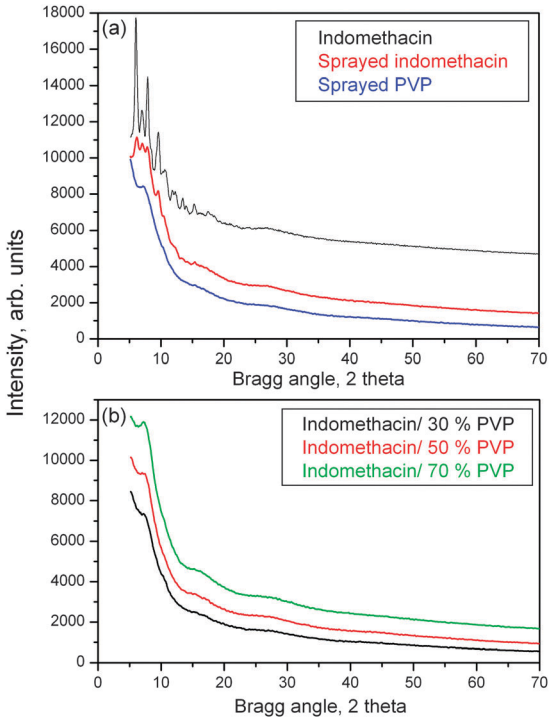


**Fig. 8** Experimental XRD patterns for crystalline indomethacin, spray dried indomethacin and polyvinylpyrrolidone (PVP) (a). Experimental XRD patterns of mixtures of spray dried indomethacin and PVP (b).

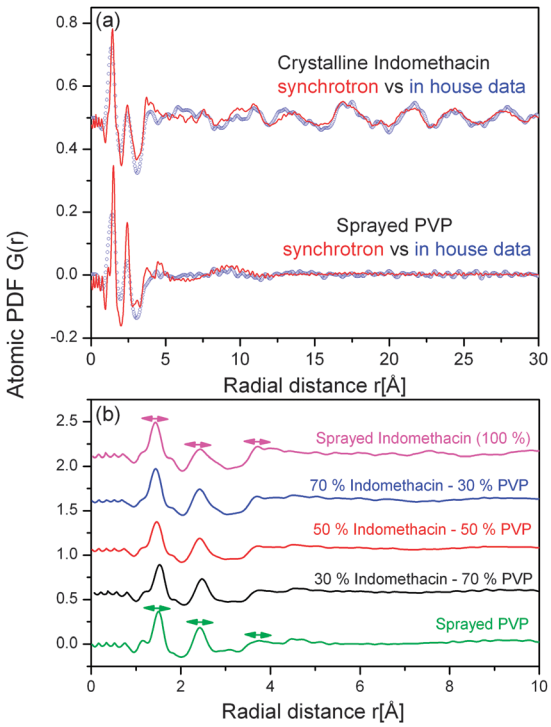


**Fig. 9** Comparison between experimental PDFs for crystalline indomethacin and sprayed PVP obtained using synchrotron and in house (Ag Kα) radiation (a). Experimental PDFs for a mixture of spray dried indomethacin and PVP. The mixing ratios are given by each data set. Horizontal arrows mark PDFs peaks whose intensities change systematically with the indomethacin/PVP mixing ratio (b).

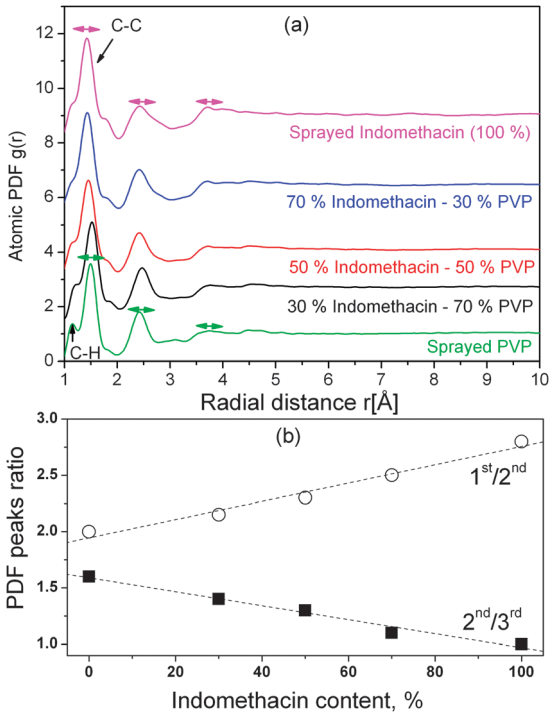


**Fig. 10** (Upper part) Experimental PDFs for a mixture of spray dried indomethacin and PVP. Peaks that vary systematically with the indomethacin/PVP ratio and so may be used to generate a calibration curve are marked with horizontal arrows; (lower part) calibration curves relating the ratio of peaks in the experimental PDFs to the volume fraction of spray dried indomethacin and PVP in their mixture.

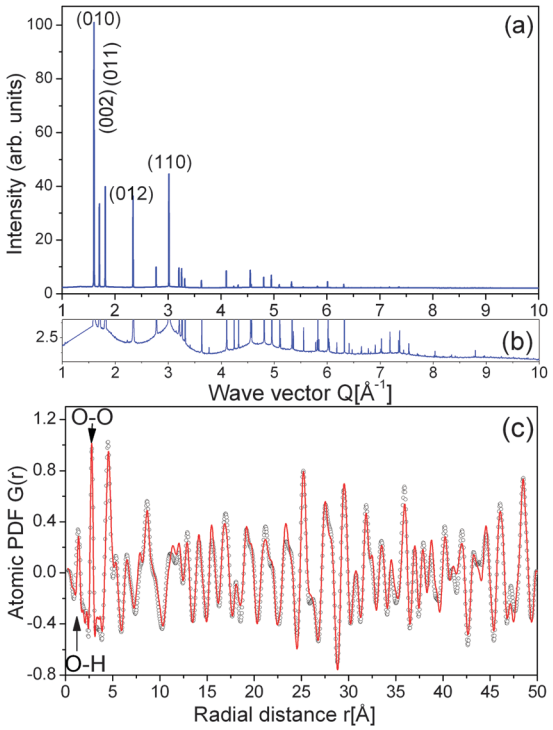


**Fig. 11** Experimental XRD patterns of Ice-Ih (line in blue). Several Bragg peaks in the XRD pattern for Ice-Ih are labeled with their Miller indices (a). Zoom in on the base of the Bragg peaks in the XRD pattern of Ice-Ih showing the presence of a substantial diffuse scattering (b). Experimental (circles) and model (line in red) atomic PDFs for Ice-Ih. The model PDF is computed from literature data[20] for the average structure of Ice-Ih not accounting for the presence of local structural distortions. The shortest interatomic distances in Ice-Ih are labeled with the corresponding atomic pairs.

first to second or the second to third PDF peaks (see Fig. 10b) can be used to generate a calibration curve for the volume concentration of indomethacin and PVP in their mixtures. The very good linear relationship between the PDFs peak derived calibration curves and the known indomethacin/PVP mixing ratio shows that intensity/area of peaks in the atomic PDF can be used to estimate the relative abundance of disordered low-$Z$ materials in mixtures of such. The approach is similar to the one applied in the traditional XRD phase analysis of polycrystalline materials where intensities of characteristic Bragg peaks of a given phase are used as representatives of the relative abundance of that phase in polycrystalline mixtures.

### 3.4 Atomic PDFs studies on liquids

Water defines life on Earth from cellular to the terrestrial levels. Yet the molecular level arrangement in water is not well understood posing problems in comprehending its very special chemical, physical and biological properties. The molecular arrangement of water has been a subject of intensive XRD studies for quite a while.[18] Here we present our recent high-energy XRD and atomic PDFs data for water.[19]

To demonstrate the often questioned sensitivity of X-rays derived PDFs to water we first measured it when frozen (250 K) at normal atmospheric pressure. The experimental XRD pattern obtained is shown in Fig. 11a. It shows a series of sharp Bragg peaks reflecting the crystalline nature of hexagonal Ice-Ih in which water freezes under ambient conditions.[19,20] A closer look at the base of the Bragg peaks (see Fig. 11(b)) reveals a strong diffuse scattering component indicating the presence of a substantial local structural disorder in Ice-Ih. The disorder involves the positioning of the hydrogen atoms about oxygen ones as well as the relative positioning of the neighboring $H_2O$ molecules with respect to each other.

The XRD data were reduced to an atomic PDF shown in Fig. 11c. As can be seen in the figure, the experimental atomic PDF for Ice-Ih shows a series of well defined peaks reflecting the presence of a sequence of very well defined coordination spheres in this crystalline material. All PDF peaks can be very well approximated with a structure model[20] featuring the well-known hexagonal structure of Ice-Ih.

XRD data for liquid water were obtained at room temperature and reduced to the so-called inter-molecular atomic PDF shown in Fig. 12. It has a first peak positioned at 2.80(1) Å followed by a small hump at about 3.5(1) Å and a clearly split second peak with two components located at 4.1(1) and 4.7(1) Å. A third broad peak is seen positioned between 6 and 8 Å. As already well established the peak positioned at 2.80(1) Å reflects the correlations between the immediate neighbor $H_2O$ molecules in water. The distinct PDF features beyond it show the presence of a specific organization of the second and further

 

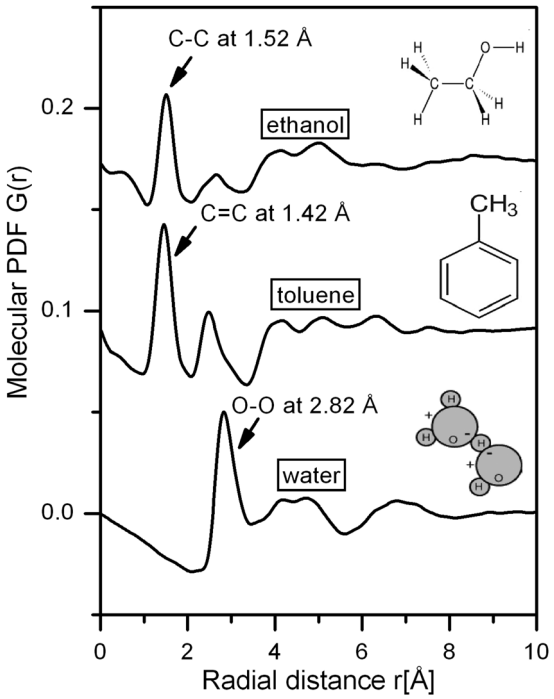


**Fig. 12** Experimental atomic PDFs for water, toluene and ethanol. The respective molecular units are shown by each data set. Selected interatomic distances occurring in the liquids are marked by arrows.

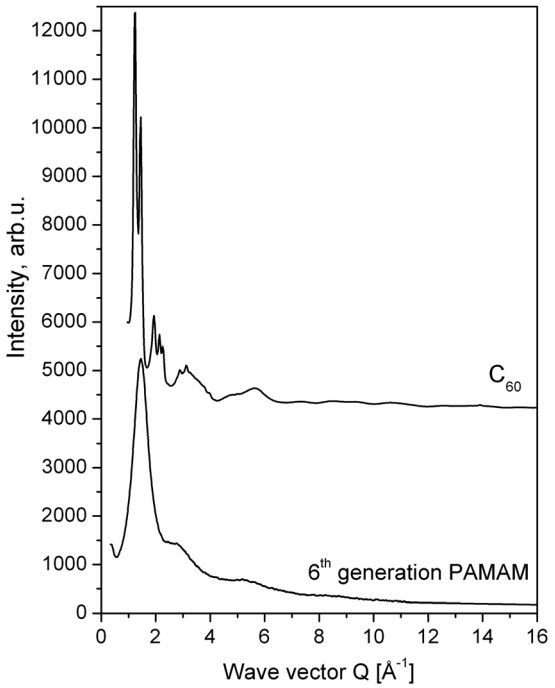


**Fig. 13** Experimental XRD patterns for fullerene ($C_{60}$) and 7th generation PAMAM dendrimers.

coordination spheres of those molecules. That organization may be well explained in terms of a structure model featuring water as a random network of tetrahedral-like units where the tetrahedral units having various degrees of perfection are further interconnected *via* hydrogen bonds in flat or buckled rings preferably made of 6, and to a lesser but definitely not negligible extent of 5 and 7 such units.[19]

Experimental atomic PDFs for ethanol ($C_2H_6O$) and toluene ($C_7H_8$) obtained by us are also shown in Fig. 12. They, as it should be, clearly show that the molecular ordering in ethanol and toluene is distinctly different from that in water. It was worth noting that the first peak in the PDF for ethanol is positioned at 1.5 Å which is the length of single C–C bonds in its molecule. For toluene this distance is at 1.41 Å reflecting the double C=C bond in its molecule. These results clearly show that high-energy XRD coupled to atomic PDFs analysis is sensitive to finest structural details not only of disordered low-*Z* solids but also of low-*Z* liquids.

### 3.5 Atomic PDFs studies of large organic molecules

Dendrimers are a novel class of macromolecules derived through a so-called 'branches-upon-branches' growing process. Branches radiate from a central core and are synthesized through a repetitive reaction sequence that guarantees a complete shell for each generation, leading to polymeric macromolecules that are globular in shape and are monodispersed.[21] The notion of nanosized cavities that are present in their structure and are vital for drug encapsulation and delivery is a central question for scientists to address. Here we show results for 7th generation PAMAM dendrimers $(C_{12}H_{28}N_2)_n$ and, as a standard sample, $C_{60}$ that is known to be a rigid molecule with a diameter of 7.1 Å.[22] Experimental high-energy XRD patterns are shown in Fig. 13. The patterns exhibit strong features at low diffraction angles and do not tell much about the molecular ordering in PAMAM and $C_{60}$. The respective atomic PDFs shown in Fig. 14 are much more informative. They exhibit a strong first peak centered at approximately 1.54 Å which is the first neighbor distance within the carbon backbone of PAMAM and $C_{60}$. In addition, the first peak in the PDFs for PAMAM dendrimers has a low-*r* shoulder at 1.1 Å. This is the hydrogen–carbon pair distance in this polymeric material. Obviously, when abundant as in PAMAM dendrimers hydrogen bonds can be clearly revealed by high-energy XRD atomic PDFs studies. $C_{60}$ is a rigid molecule consisting of 60 carbon atoms bonded in a nearly spherical configuration that encloses a cavity with a diameter of 7.1 Å. Since the molecule is rigid, all interatomic distances within it are well defined and the corresponding peaks in the atomic PDF are well resolved (Fig. 14, up). At room temperature $C_{60}$ molecules spin almost freely in their crystal positions, so they look like soccer balls. The correlation between the carbon atoms from the neighboring balls is lost. As a result, starting at 7.1 Å, the atomic PDF turns into a low-frequency oscillation reflecting the ''ball–ball'' correlations. A model PDF calculated from crystal structure data for fullerene (red line in Fig. 14) approximates the experimental data very well attesting to the very good quality of the results of high-energy XRD and PDFs technique deliver. The PDF for PAMAM dendrimers too shows a series of well defined peaks extending to approx. 10 Å followed by an almost featureless tail. With fullerene the change in the PDF shape at 7.1 Å is very sharp

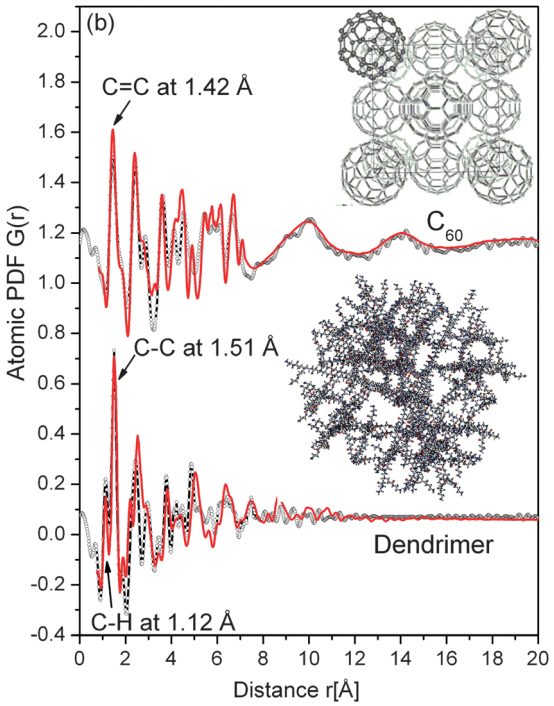


**Fig. 14** Experimental (symbols) atomic PDFs for fullerene ($C_{60}$) and 7th generation PAMAM dendrimers extracted from the XRD patterns of Fig. 13. Shortest interatomic distances in the two materials are marked with arrows. Fits (solid line) to the experimental PDFs are based on the structure models shown by the respective data sets.

since the intra and intermolecular correlations do not overlap. This behavior reflects the presence of a 3D ordered array of identical "rigid balls/cavities" (Fig. 14, top right). In PAMAM dendrimers the change in the shape of PDF is not so abrupt indicating that the intra and intermolecular correlations overlap to a certain extent, *i.e.* the PAMAM branches may approach each other at various distances. This behavior implies a smaller degree of atomic ordering and the presence of cavities of somewhat different dimensions (Fig. 14, bottom right). Indeed extensive computer simulations[21] based on the experimental PDFs data reveal that branches inside dendrimers are not arranged in exactly concentric shells but in a semi-regular pattern forming a network-like structure. This network is riddled with cavities ranging from 5 to 15 Å in diameter and some of the cavities are joined into channels connecting the PAMAM's surface and core. Thus by using high-energy XRD and the atomic PDF technique it is possible to provide direct structural evidence that PAMAM dendrimers are relatively well ordered at the atomic scale and with a relatively open interior. Due to their unique atomic-scale structure dendrimers can accommodate small molecules and atomic clusters rendering them very suitable for bio-imaging and drug delivery applications.

### 3.6 Atomic PDFs studies on hydrogen storage materials

Hydrogen is one of the most promising energy storing materials. It does not add to the environmental pollution when generated from renewable sources. For applications in the automobile industry its compact storage and efficient release are important issues. Among other possibilities, storage as a solid hydride is attractive from safety and gravimetric points of view. A material of great interest is ammonia borane ($BH_3NH_3$). Hydrogen can be readily generated either by hydrolysis or by heating ammonia borane above 80 °C. Knowledge of the atomic-scale structure of ammonia borane thus becomes important since it is directly related to the hydrogen release mechanism. The structure of ammonia borane and its storage in inorganic scaffolds have been investigated by several groups.[23,24] Now it is firmly established that at low (below 220 K) temperature it crystallizes into an orthorhombic space group ($Pmn2_1$). Motion of the $-BH_3$ and $-NH_3$ groups increases with temperature and at room temperature ammonia borane adopts a body centered tetragonal structure (S.G. *I4mm*). This structural picture is, however, obtained from traditional analysis of powder XRD and so is a representative of the average positions of $-BH_3$ and $-NH_3$ groups only. An experimental high-energy XRD pattern of ammonia borane taken at room temperature is shown in Fig. 15 (upper part). The respective atomic PDF is shown in Fig. 15 (lower part) together with the ammonia borane molecule. The experimental PDF reflects very well the B/N–H bonds at 1.1 Å and the B–N bonds at 1.6 Å, again proving the great sensitivity of high-energy XRD and atomic PDFs to the presence of well-defined molecules in low-*Z* materials. A model based on the average tetragonal (S.G. *I4mm*) structure is compared to the experimental PDF data (red line in Fig. 15; bottom part). The model approximates

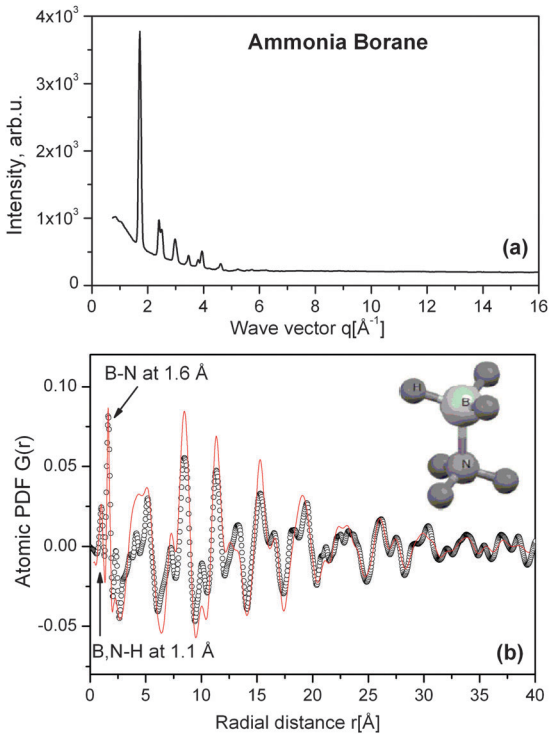


**Fig. 15** Experimental XRD patterns of ammonia borane (a). Experimental (symbols) and model (line) atomic PDFs for ammonia borane. The ammonia borane $BH_3NH_3$ molecule is shown as well. Shortest interatomic distances in ammonia borane are marked with arrows (b).

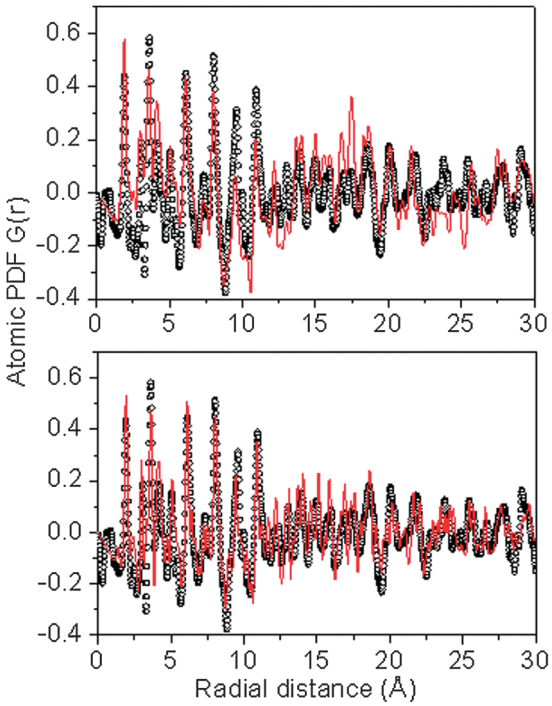


**Fig. 16** Comparison between the experimental PDF for the $PANI_x{\cdot}V_2O_5$ composite (symbols) and model PDFs for the $V_2O_5$ matrix without (solid line, upper part) and with (solid line, lower part) polyaniline intercalated between the V–O layers as shown in Fig. 17.

the major peaks in the experimental data but misses several fine PDF details indicating that the local structure of ammonia borane at room temperature departs from the average one. More studies are necessary to reveal the exact atomic ordering in ammonia borane close to the temperature of hydrogen release (80 °C) so that its hydrogen storage properties are better understood and utilized. High-energy XRD and atomic PDFs analysis may prove very useful in this investigation.

### 3.7 Atomic PDFs studies on composites of low-*Z* and high-*Z* materials

In recent years, conducting organic–inorganic composites have attracted much attention because of their properties and a wide variety of potential applications. Of particular interest are composites based on polymeric polyaniline (PANI) and $V_2O_5$ xerogel. Here the combination of the conducting properties of PANI and the inorganic host results in a nanophase material with very valuable charge- and ion-transport properties. To understand and so make a better use of these properties a detailed knowledge about the atomic scale structure of the $PANI_x{\cdot}V_2O_5$ composite is needed. Traditional XRD is helpless in the case of organic–inorganic nanophase composites since they lack the extended structural order and periodicity of conventional crystals. By employing high-energy XRD and atomic PDFs analysis the structure of $PANI_x{\cdot}V_2O_5$ can be determined in very good detail.[25] The experimental atomic PDF for $PANI_x{\cdot}V_2O_5$ obtained by high-energy XRD experiments is shown in Fig. 16. It is rich in sharp features indicating that this composite

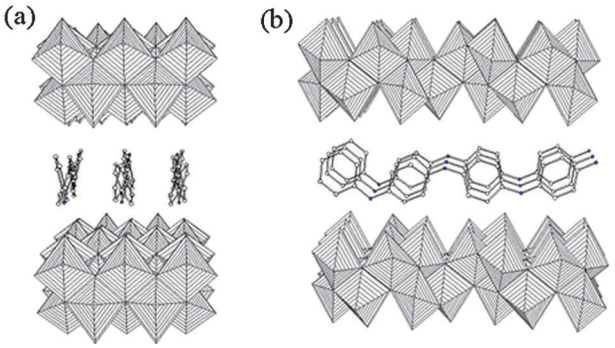


**Fig. 17** Structure of the $PANI_x{\cdot}V_2O_5$ composite as determined by computer simulations guided by experimental atomic PDFs. The structure features double layers of octahedral V–$O_6$ units (shaded) with polymeric PANI chains intercalated between them.

material has a very well defined local atomic ordering. A comparison between the experimental PDF for $PANI_x{\cdot}V_2O_5$ with that for pure $V_2O_5$ xerogel is shown in Fig. 16, upper part. It reveals that the $PANI_x{\cdot}V_2O_5$ composite shares several of the structural features of the inorganic host indicating that the structural integrity of the latter is preserved in the former. The intensity of several peaks in the experimental PDF is, however, badly missed indicating that a structure model based on the inorganic host alone is not capable of explaining the experimental data.

When PANI polymeric chains are included in the structure model in a way shown in Fig. 17 the agreement between the experimental and model PDF data is improved very substantially. The result shows that high-energy XRD and atomic PDF analysis can be quite sensitive to the low-*Z* component of low-*Z*(polymeric)–high-*Z*(inorganic oxides) composites. In the particular case of a $PANI_x{\cdot}V_2O_5$ composite this non-traditional experimental approach helps reveal[25] the atomic-scale structure as a regular arrangement of double layers of $V_2O_5$ octahedra sandwiching PANI chains in the way shown in Fig. 17. Note that other orientations of the PANI chains with respect to the $V_2O_5$ layers have been tested but only the one shown in Fig. 17 was found to be consistent with the experimental PDF data.[25] Other successful studies on the low-*Z* component in low-*Z*/high-*Z* materials are also known.[26]

## 4. Conclusions

High-energy XRD coupled to atomic PDFs analysis is a very useful experimental technique for characterization of disordered low-*Z* materials both in solid (*e.g.* $C_{60}$ fullerene) and liquid states (*e.g.* water, ethanol, toluene). It can be used for qualitative (*e.g.* cellulose derivatives, nanophase carbons) and quantitative (*e.g.* amorphous pharmaceuticals) material's phase analysis, revealing fine structural features (*e.g.* hydrogen bonds in ammonia borane), the presence of defects (*e.g.* as in ball milled carbons) and can provide a firm basis for atomic-scale structure simulations (*e.g.* PAMAM dendrimers). The technique can be sensitive to the low-*Z* component of low-*Z*–high-*Z* mixtures (*e.g.* PANI in $V_2O_5$), requiring a relatively small amount of samples,

studies in various environments and can be practiced both on in-house equipment (Mo or Ag radiation) and at synchrotron radiation facilities. Given this the technique should find wide spread utility.

## Acknowledgements

VP acknowledges help from DOE *via* DE-SC0006877, NSF and ARL. Work at APS has been supported by DOE under Contract DE-AC02-06CH11357.

## References

1 B. E. Warren, *Phys. Rev. B: Solid State*, 1934, **45**, 657.
2 T. Egami and S. J. L. Billinge, in *Underneath the Bragg peaks: Structural Analysis of Complex Materials*, Pergamon Press, Elsevier Ltd., 2003.
3 V. Petkov, *Mater. Today*, 2008, **11**, 28.
4 P. K. Klug and L. E. Alexander, in *X-Ray Diffraction Procedures: For Polycrystalline and Amorphous Materials*, John Wiley & Sons Inc., 2nd edn, 1974.
5 C. N. J. Wagner, *J. Vac. Sci. Technol.*, 1969, **6**, 650.
6 D. A. Keen, *J. Appl. Crystallogr.*, 2001, **34**, 172.
7 R. Young, in *Cellulose structure modification and hydrolysis*, Wiley, New York, 1986.
8 G. M. Brown, D. C. Rohrer, B. Berking, C. A. Beevers, R. O. Gould and R. Simpson, *Acta Crystallogr., Sect. B: Struct. Sci.*, 1972, **28**, 3145.
9 H. Nagase, N. Ogawa, T. Endo, M. Shoro, H. Ueda and M. Sakurakai, *J. Phys. Chem.*, 2008, **112**, 9105.
10 V. Petkov, A. Timmons, J. Camardese and Y. Ren, *J. Phys.: Condens. Matter*, 2011, **23**, 435003.
11 V. Petkov, R. G. DiFranchesco, S. J. L. Billinge, M. Acharya and H. C. Foley, *Philos. Mag. B*, 1999, **79**, 1519.
12 M. Sato and Th. J. Webster, *Expert Rev. Med. Devices*, 2004, **1**, 1.
13 E. Serrano, G. Rus and J. Garcıa-Martınez, *Renewable Sustainable Energy Rev.*, 2009, **13**, 2327.
14 S. Smith and R. L. Snyder, *J. Appl. Crystallogr.*, 1979, **12**, 60.
15 D. W. M. Hofmann and L. Kuleshova, *J. Appl. Crystallogr.*, 2005, **38**, 86.
16 K. Nagapundi and J. Jona, *Curr. Bioact. Compd.*, 2008, **4**, 213.
17 N. Jagadeesh and A. Nangia, *Cryst. Growth Des.*, 2011, **11**, 26222.
18 G. Hura, J. M. Sorenson, R. M. Glaeser and T. Head-Gordon, *J. Phys. Chem.*, 2000, **113**, 9140.
19 V. Petkov, Y. Ren and M. Suchomel, *J. Phys.: Condens. Matter*, 2012, **24**, 155102.
20 G. Malenkov, *J. Phys.: Condens. Matter*, 2009, **21**, 283101.
21 V. Petkov, V. Parvanov, D. Tomalia, D. Swanson, D. Bergstrom and T. Vogt, *Solid State Commun.*, 2005, **134**, 671.
22 Th. Proffen, S. J. L. Billinge, T. Egami and D. Louca, *Z. Kristallogr.*, 2003, **218**, 132; A. K. Soper, W. I. F. David, D. S. Sivia, T. J. S. Dennis, J. P. Hare and K. Prassides, *J. Phys.: Condens. Matter*, 1992, **4**, 6087; C. Elschner, A. A. Levin, L. Wilde, J. Grenzer, C. Schroer, K. Leo and M. Riede, *J. Appl. Crystallogr.*, 2011, **44**, 983.
23 M. E. Bowden, G. J. Gainsford and W. T. Robinson, *Aust. J. Chem.*, 2007, **60**, 149.
24 H. Kim, A. Karkamkar, T. Autrey, P. Chupas and Th. Proffen, *J. Am. Chem. Soc.*, 2009, **131**, 13749.
25 V. Petkov, V. Parvanov, P. Trikalitis, Ch. Malliakas, T. Vogt and G. Kanatzidis, *J. Am. Chem. Soc.*, 2005, **127**, 8805.
26 K. W. Chapman, P. J. Chupas and C. J. Kepert, *J. Am. Chem. Soc.*, 2005, **127**, 15630.

 